Near-wall modelling in Eulerian-Eulerian simulations

M. Riella[a,*], R. Kahraman[b], G. R. Tabor[a]

[a] *College of Engineering, Mathematics and Physical Sciences, University of Exeter, North Park Road, Exeter, EX4 4QF, UK*

[b] *HiETA Technologies Ltd, Bristol & Bath Science Park, Dirac Crescent, Emersons Green, Bristol, BS16 7FR, UK*

Abstract

The near-wall region in turbulent Eulerian-Eulerian (E-E) simulations has hitherto received little to no attention. A standard approach to modelling this region is through the employment of single-phase wall-functions in the fluid-phase and it is unclear whether such an approach is capable of capturing the turbulent fluid-particle interaction in the near-wall region. In order to both investigate and alleviate E-E models reliance on single-phase wall-functions we propose an E-E elliptic relaxation model to account for the near-wall non-homogeneity which arises in wall-bounded flows. The proposed model is derived within an E-E framework and enables the full resolution of the boundary layer and arbitrary wall sensitivity. The model is then compared against the conventional $k_f - \varepsilon_f$ turbulence model with standard single-phase wall-functions. Additionally, the modelling is compared against a low-Re number turbulence model. The elliptic relaxation model is implemented within the open-source CFD toolbox OpenFOAM, applied to a vertical downward-facing channel and validated against the benchmark experimental data of Kulick et al.

*Corresponding author
Email address: `mjr214@exeter.ac.uk` (M. Riella)

[20]. Model results show marked improvements over the conventional turbulence model across mean flow and turbulence statistics predictions. The use of conventional single-phase wall functions were shown to negatively impede on the prediction of the velocity covariance coupling term and as a result the particle fluctuation energy. Moreover, this also lead to an underestimation of the near-wall volume fraction accumulation. Finally, the elliptic relaxation model, E-E model and accompanying validation cases are made open-source.
Keywords: `v2-f`, `Boundary-layer`, `E-E`, `Near-wall`

1. Introduction

Many researchers have investigated turbulent wall-bounded fluid-particle flow through experimentation [4, 11, 15, 20, 23, 49]. Owing to their turbulent nature such flows exhibit complex physical behaviour giving rise to turbulence modulation which can be caused by: particle-particle, fluid-particle and/or particle-wall interactions. Thus, research has been ongoing to understand and model these phenomena; most of which are common in engineering processes, e.g. pneumatic conveyance and coal particle combustion. The aforementioned experimental studies provide invaluable physical insights and validation data for the development of predictive models. One notable study is that of Kulick et al. [20] which has received considerable attention from researchers developing, predominantly Euler-Lagrange (E-L), models [19, 25, 42, 47, 51, 52, 54]. This study is particularly attractive as there are several particle classes giving rise to various particle-fluid and particle-wall interactions which contribute to turbulence modulation.

Having identified the aspects of physical behaviour which are significant in these flows, researchers can investigate them separately in a reductionist approach. We now highlight some studies that contribute to the understanding of particle behaviour within the case of Kulick et al. [20]; starting with the so-called feedback-force of the particle phase on the fluid turbulence in the flow. Vreman [51] recently examined the effect of the mean feedback-force and how it is exacerbated by wall roughness. An increase in wall roughness enhances turbulence attenuation i.e. a reduction in fluid-phase velocity fluctuations. This explains the over prediction of the mean particle velocities seen in previous studies Kubik and Kleiser [19], Wang and Squires [52], Yamamoto et al. [54] as smooth walls were simulated.

Another phenomenon that has been investigated is turbophoresis, which refers to the tendency of particles in the flow to migrate towards regions of lower turbulence. The turbophoresis force is responsible for particles drifting from regions of high turbulence intensity to low turbulence intensity [27, 35], which often results in particles accumulating in the near-wall region characterised by low-speed streaks [32, 34]. This accumulation in the near-wall region is referred to as deposition and has been researched numerically by [24, 27, 28, 30]. One of the first models for particle deposition by Young and Leeming [55] showed that the turbophoretic velocity depends on the gradient of wall-normal fluctuating velocities and provided one of the first physical basis for explaining the turbophoresis force. Strömgren et al. [47] investigated the effect of the turbophoresis force within an Eulerian-Eulerian (E-E) framework and found that even for small volume fractions, $\alpha_p = 2\text{x}10^{-4}$, two-way coupling effects are non-negligible and the near-wall region may require special attention. This is due to the accumulation of particles in the near-wall region i.e viscous sub layer, leading to higher volume fractions in which two-way coupling effects become more relevant [14].

In turbulent single-phase simulations the near-wall region is typically modelled. Wall functions are applied to turbulence quantities, ε_f & ν_{ft} with a zero gradient condition given to k_f, in order to avoid the computational overhead of detailed resolution of the flow in the near-wall region. Such wall functions are based on the law-of-the-wall, which is that the dimensionless velocity, u^+ varies through some function expressed generically as, $u^+ = f_{log}(\mathrm{y}^+)$. The function f_{log} is logarithmic representing the outer log-law region of the turbulent boundary layer. This corresponds to the constant-stress layer in which the turbulent shear stress is proportional to the friction velocity [45]. In turbulent quantity terms this means that the production and dissipation of turbulent kinetic energy are equal.

The law-of-the-wall is assumed to be universal and is found through dimensional reasoning, this then leads to a description of the near-wall region through dimensionless variables i.e. velocity and wall-normal coordinates. The dimensionless wall-normal coordinate is defined as $\mathrm{y}^+ = \mathrm{y}u_\tau/\nu_f$ and the log-law is applicable in the range of $30 < \mathrm{y}^+ < 300$, this then gives a universal relation that can be applied to turbulent wall-bounded flows. This criterion places a requirement on the first computational cell i.e. the distance of the cell centre must be further than $\mathrm{y}^+ > 30$. As can already be deduced, the calculation of y^+ depends on the friction velocity, which is not known *a priori*. Hence, this quantity is estimated prior to calculation using standard skin friction relations and informs mesh generation. This approach then sacrifices near-wall resolution for a computationally cheaper simulation. An important assumption about the nature of the law-of-the-wall has been made throughout i.e. its universal nature. This is in fact not true as it has been shown experimentally that the boundary layer is affected by adverse pressure gradients and geometric changes [16].

The viability of single-phase wall functions applied to multiphase simulations has attracted some interest from researchers. A theoretical study by Rizk and Elghobashi [40] showed that increasing volume fraction can adversely effect the mean profile prediction. It was found that with increasing particle volume fraction the log layer broke down resulting in an overestimation. Interestingly, a similar relationship between an increasing mass loading and a reduction in the mean log-layer momentum was recently found experimentally by Saber et al. [44]. Benyahia et al. [2] included the effect of the particle phase directly into the wall function. An additional term that contains the drag and velocity fluctuation covariance is introduced in the log-law relation. This formulation allows the presence of the particles to influence the velocity profile, although when extended to more complex geometries the short-comings of single-phase wall functions remain.

Attempts to circumvent the reliance on single-phase wall functions have been made by several authors [3, 6, 40, 57] in which a low-Re number turbulence model is used. This allows the transport equations to be integrated up to the wall. This approach has proven fruitful for numerous authors as without the use of wall functions, the presence of the particles within the boundary layer can exert their influence [40, 57]. The low-Re turbulence model uses a damping function and a near wall correction of Kolmogorov scaling [31]. The damping of the viscosity can be somewhat arbitrary and validated on relatively simple flow leading to a range of different models [5, 21, 41, 46] with an extensive summary found in Patel et al. [31]. The damping functions used in Patel et al. [31] are often non-linear and can lead to numerical stiffness further complicating their application.

Durbin [8] proposes another way of accounting for wall-induced non-homogeneity. The quantity $\overline{v_f^2}$, which represents the turbulence-stress normal to streamlines, is introduced. This quantity is derived from the exact Reynolds-stress transport equation and contains a source term that accounts for the redistribution of turbulence kinetic energy. This inclusion explicitly accounts for the wall-induced non-homogeneity and enables the wall-normal component to be dampened. The energy redistribution is governed by an *elliptic relaxation* equation f, that is free of geometric dependence or arbitrary fitting. The $\overline{v_f^2} - f$ elliptic relaxation model has been validated across various challenging single-phase flows [1, 7, 26, 29, 48] highlighting the benefit of such a modelling technique.

There are two closely linked issues with the current E-E modelling approaches: the modelling of the near-wall region, through single-phase wall functions, and the subsequent consequences of such an approach i.e. the prediction of turbulence modulation and turbophoresis. In this work we seek to investigate this by carrying out a side-by-side comparison of a conventional E-E simulation method with a newly-derived elliptic relaxation model in which the near-wall region has been resolved. The main aim then is to reveal the consequences of modelling the near-wall region whilst proposing new modelling to circumvent these consequences.

We begin at a recently proposed E-E model, namely the Reynolds-Averaged Two-Fluid Model of Fox [13]. This approach has proven particularly fruitful in modelling high Re number flows due to the inclusion of particle inertia induced energy separation (see Février et al. [12], Fox [13]) and has lead to a high level of validation [38, 39]. The elliptic relaxation model of Durbin [8] is derived within the RA-TFM framework and applied to the vertical downward facing channel of Kulick et al. [20]. The elliptic relaxation model alleviates the use of wall functions and/or the use of ad-hoc damping functions and their geometric dependency. To ascertain the consequences of a conventional E-E simulation, the RA-TFM with the solution of the

$k_f - \varepsilon_f$ model, and is compared and contrasted against the newly proposed elliptic relaxation model, $\overline{v_f^2} - f$. Moreover, results are also compared against the low Re number model of Launder and Sharma [21] in order to facilitate a boundary layer resolved comparison.

2. Numerical model

We begin at the RA-TFM of Fox [13], and as we are interested in extending the fluid-phase turbulence modelling we present the fluid- and particle-phase governing equations as well as the particle-phase fluctuation energy equations in Table 1. We have neglected coupling through buoyancy due to the high density ratios simulated in this work and therefore, we begin at the fluid-phase turbulence equations.

The turbulent kinetic energy transport equation for the fluid-phase takes the form:

$$\begin{aligned}\frac{\partial(\alpha_f\rho_f k_f)}{\partial t} + \nabla\cdot(\alpha_f\rho_f k_f \mathbf{u}_f) = \nabla\cdot\Big(\mu_t + \frac{\mu_{ft}}{\sigma_{fk}}\Big)\nabla k_f + \alpha_f\rho_f\Pi_f - \alpha_f\rho_f\varepsilon_f \\ +2\beta(k_{fp} - k_f).\end{aligned} \tag{1}$$

The turbulent kinetic energy dissipation transport equation reads:

$$\begin{aligned}\frac{\partial(\alpha_f\rho_f \varepsilon_f)}{\partial t} + \nabla\cdot(\alpha_f\rho_f \varepsilon_f \mathbf{u}_f) = \nabla\cdot\Big(\mu_t + \frac{\mu_{ft}}{\sigma_{fk}}\Big)\nabla \varepsilon_f + \frac{\varepsilon_f}{k_f}\Big[C_1\alpha_f\rho_f\Pi_f - C_2\alpha_f\rho_f\varepsilon_f\Big] \\ +2C_3\beta(\varepsilon_{fp} - \varepsilon_f).\end{aligned} \tag{2}$$

The first term on the RHS is the fluid-phase turbulent kinetic energy/dissipation flux. The second term, Π_f is the kinetic energy production due to mean shear with the third term being the turbulent kinetic energy dissipation. The remaining term is the coupling terms due to velocity covariance (see Table 9) and is a measure of how correlated the two phases are. This provides the primary coupling mechanism in this work as the two phases are only coupled through drag.

These two equations make up the conventional $k_f - \varepsilon_f$ turbulence model with model constants, largely taken from compressible turbulence modelling [43], found in Table 3. The complete set of equations that make up the RA-TFM are found in Table 1 and the equations associated with the low Re number model of Launder and Sharma [21] can be found in Table 2.

Table 1: RA-TFM governing equations and the particle fluctuation energy equations.

$$\frac{\partial(\alpha_p\rho_p)}{\partial t} + \nabla\cdot(\alpha_p\rho_p\mathbf{u}_p) = 0 \tag{3}$$

$$\frac{\partial(\alpha_f\rho_f)}{\partial t} + \nabla\cdot(\alpha_f\rho_f\mathbf{u}_f) = 0 \tag{4}$$

$$\begin{aligned}\frac{\partial(\alpha_p\rho_p\mathbf{u}_p)}{\partial t} + \nabla\cdot(\alpha_p\rho_p\mathbf{u}_p\mathbf{u}_p) = \nabla\cdot\Big(2(\mu_p+\mu_{pt})\overline{\mathbf{S}}_\mathbf{p}\Big) + \beta\Big[(\mathbf{u}_f-\mathbf{u}_p) - \frac{\nu_{ft}}{\mathrm{Sc}_{fs}\alpha_p\alpha_f}\nabla\alpha_p\Big]\\ -\nabla p_p - \alpha_p\nabla p_f + \alpha_p\rho_p\mathbf{g}\end{aligned} \tag{5}$$

$$\begin{aligned}\frac{\partial(\alpha_f\rho_f\mathbf{u}_f)}{\partial t} + \nabla\cdot(\alpha_f\rho_f\mathbf{u}_f\mathbf{u}_f) = \nabla\cdot\Big(2(\mu_f+\mu_{ft})\overline{\mathbf{S}}_\mathbf{f}\Big) + \beta\Big[(\mathbf{u}_p-\mathbf{u}_f) + \frac{\nu_{ft}}{\mathrm{Sc}_{fs}\alpha_p\alpha_f}\nabla\alpha_p\Big]\\ -\alpha_f\nabla p_f + \alpha_f\rho_f\mathbf{g}\end{aligned} \tag{6}$$

$$\begin{aligned}\frac{\partial(\alpha_p\rho_p k_p)}{\partial t} + \nabla\cdot(\alpha_p\rho_p k_p\mathbf{u}_p) = \nabla\cdot\Big(\mu_p + \frac{\mu_{pt}}{\sigma_{pk}}\Big)\nabla k_p + \alpha_p\rho_p\Pi_p - \alpha_p\rho_p\varepsilon_p\\ +2\beta(k_{fp}-k_p)\end{aligned} \tag{7}$$

$$\begin{aligned}\frac{\partial(\alpha_p\rho_p\varepsilon_p)}{\partial t} + \nabla\cdot(\alpha_p\rho_p\varepsilon_p\mathbf{u}_p) = \nabla\cdot\Big(\mu_p + \frac{\mu_{pt}}{\sigma_{p\varepsilon}}\Big)\nabla\varepsilon_p + \frac{\varepsilon_p}{k_p}\Big[C_1\alpha_p\rho_p\Pi_p - C_2\alpha_p\rho_p\varepsilon_p\Big]\\ +2C_3\beta(\varepsilon_{fp}-\varepsilon_p)\end{aligned} \tag{8}$$

$$\begin{aligned}\frac{3}{2}\Big[\frac{\partial(\alpha_p\rho_p\Theta_p)}{\partial t} + \nabla\cdot(\alpha_p\rho_p\Theta_p\mathbf{u}_p)\Big] = \nabla\cdot\Big(\kappa_\Theta + \frac{3\mu_{pt}}{2Pr_{pt}}\Big)\nabla\Theta_p + 2\mu_p\overline{\mathbf{S}}_\mathbf{p} : \overline{\mathbf{S}}_\mathbf{p}\\ -p_p\nabla\cdot\mathbf{u}_p + \alpha_p\rho_p\varepsilon_p - 3\beta\Theta_p - \gamma\end{aligned} \tag{9}$$

Table 2: Low Re number turbulence model of Launder and Sharma [21].

$$\frac{\partial(\alpha_f\rho_f k_f)}{\partial t} + \nabla\cdot(\alpha_f\rho_f k_f \mathbf{u}_f) = \nabla\cdot\Big(\mu_f + \frac{\mu_{ft}}{\sigma_{fk}}\Big)\nabla k_f + \alpha_f\rho_f\Pi_f - \alpha_f\rho_f\varepsilon_f + 2\beta(k_{fp} - k_f) \tag{10}$$

$$\frac{\partial(\alpha_f\rho_f\widetilde{\varepsilon})}{\partial t} + \nabla\cdot(\alpha_f\rho_f\widetilde{\varepsilon}\mathbf{u}_f) = \nabla\cdot\Big(\mu_f + \frac{\mu_{ft}}{\sigma_{f\epsilon}}\Big)\nabla\widetilde{\varepsilon} + C_1\alpha_f\rho_f\Pi_f\frac{\widetilde{\varepsilon}_f}{k_f} - C_2\alpha_f\rho_f f_2\frac{\widetilde{\varepsilon}^2}{k_f} + E + 2C_3\beta(\varepsilon_{fp} - \widetilde{\varepsilon}_f) \tag{11}$$

where

$$\mu_{ft} = c_\mu f_\mu \rho_f \frac{k_f^2}{\widetilde{\varepsilon}}$$

$$\varepsilon_f = \widetilde{\varepsilon} + D$$

$$f_\mu = \exp\Big(\frac{-3.4}{(1+R_T/50)^2}\Big)$$

$$f_2 = 1 - 0.3\exp(-R_T^2)$$

$$D = 2\mu_f(\nabla\sqrt{k_f})^2$$

$$E = 2\mu_f\mu_{ft}(\nabla^2\mathbf{u}_f)^2$$

$$R_T = \frac{k_f^2}{\nu_f\widetilde{\varepsilon}}$$

Table 3: $k_f - \varepsilon_f$ model constants.

C_1	C_2	C_3	β_k	β_ε	$C_{f\mu}$	$C_{p\mu}$	$\sigma_{f\epsilon}$	σ_{fk}
1.44	1.92	1	1	1	0.09	0.09	1.3	1

2.1. Fluid-phase elliptic relaxation model

We begin at the exact RA Reynolds stress transport equation for the fluid-phase and for the sake of brevity the derivation is presented in the Appendix. The equation then reads:

$$\begin{aligned}\frac{\partial\langle\alpha_f\rangle\langle\mathbf{u}_f'''\otimes\mathbf{u}_f'''\rangle_f}{\partial t}+\nabla\cdot\langle\alpha_f\rangle\langle\mathbf{u}_f\rangle_f\otimes\langle\mathbf{u}_f'''\otimes\mathbf{u}_f'''\rangle_f &= -\nabla\cdot\langle\alpha_f\rangle\langle\mathbf{u}_f'''\otimes\mathbf{u}_f'''\otimes\mathbf{u}_f'''\rangle_f\\ &-\underbrace{\langle\alpha_f\rangle(\langle\mathbf{u}_f'''\otimes\mathbf{u}_f'''\rangle_f\cdot\nabla\langle\mathbf{u}_f\rangle_f)}_{\text{Production}}+\frac{1}{\rho_f}\nabla\cdot\langle\overline{\boldsymbol{\sigma}}_f\otimes\mathbf{u}_f'''\rangle-\frac{1}{\rho_f}\nabla\langle p_f\mathbf{u}_f'''\rangle\\ +\underbrace{\frac{1}{\rho_f}\langle p_f\nabla\mathbf{u}_f'''\rangle}_{\text{pressure strain, }\phi_{yy}}-\underbrace{\frac{1}{\rho_f}\langle\overline{\boldsymbol{\sigma}}_f\cdot\nabla\mathbf{u}_f'''\rangle}_{\text{dissipation, }\varepsilon_{yy}}&+\langle\alpha_f\rangle\beta(\underbrace{\langle\mathbf{u}_f'''\otimes\mathbf{u}_p''\rangle_p-\langle\mathbf{u}_f'''\otimes\mathbf{u}_f'''\rangle_p}_{\text{velocity correlations}}).\end{aligned} \tag{12}$$

Firstly, as we intend to arrive at a transport equation for an 'imaginary' wall-normal stress component a caveat is worth mentioning. If one considers the production term in any classic eddy-viscosity model, the production term is proportional to the mean flow gradient - importantly in the stream-wise direction. This means that the turbulent kinetic energy is produced by the stream-wise mean flow gradients. Consequently, in the wall-normal direction the production term vanishes.

The velocity correlations which arise due to phase coupling are modelled analogously to those terms found in the $k_f-\varepsilon_f$ transport equations. We set the covariance of the fluctuations $\langle\mathbf{u}_f'''\otimes\mathbf{u}_p''\rangle_p=\overline{v_{fp}^2}=\beta_v\sqrt{\overline{v_p^2}\,\overline{v_f^2}}$, where $\overline{v_p^2}=2/3k_p$ owing to its definition. The correlation factor, $\beta_v=1$ along with the correlation factors found in the transport equations for turbulent kinetic energy and dissipation (see Table 9) are all set to 1. This is a crude first approximation and the correlation factor should depend on both mass loading and Stokes number. This is out of the scope of this work but only a weak dependency through the relatively low mass loadings is expected.

Following the approach used in classic eddy-viscosity turbulence models, the divergence terms appearing in the transport equation are closed by the eddy-viscosity approximation [33]. This reads as:

$$\nabla \cdot \left[\frac{\mu_{ft}}{\sigma_{fk}} \nabla \langle \mathbf{u}_f''' \otimes \mathbf{u}_f''' \rangle_f \right] \approx -\nabla \cdot \langle \alpha_f \rangle \langle \mathbf{u}_f''' \otimes \mathbf{u}_f''' \otimes \mathbf{u}_f''' \rangle_f + \frac{1}{\rho_f} \nabla \cdot \langle \overline{\boldsymbol{\sigma}}_f \otimes \mathbf{u}_f''' \rangle - \frac{1}{\rho_f} \nabla \langle p_f \mathbf{u}_f''' \rangle. \tag{13}$$

Finally, the terms left to close are the pressure strain and dissipation terms. These terms are explicitly modelled in the $\overline{v_f^2} - f$ model equations and are grouped into a source term denoted $k_f f$,

$$k_f f = \underbrace{\phi_{yy}}_{\text{pressure strain}} - \underbrace{\varepsilon_{yy}}_{\text{dissipation}} + \alpha_f \rho_f 6 \frac{\overline{v_f^2}}{k_f} \varepsilon_f. \tag{14}$$

The source term effectively redistributes turbulence energy from the stream-wise Reynolds stress component to the wall-normal component. This is intuitive as previously discussed, when one considers a fully developed turbulent boundary layer as the wall-normal Reynolds stress component's production is zero due to the mean stream-wise flow gradient. This means that turbulence energy can only enter the wall-normal component through redistribution. The original form of the source term has been shown to overproduce in regions relatively far away from the wall and the correction of Davidson et al. [7] is thus employed, this then reads

$$\overline{v_f^2}_{source} = \min\left\{ k_f f,\ -\frac{1}{T}\left[(C_1 - 6)\overline{v_f^2} - \frac{2k_f}{3}(C_1 - 1) \right] + C_2 \Pi_f \right\}. \tag{15}$$

Finally, setting the wall-normal component of the fluid-phase Reynolds stress tensor $\langle \mathbf{u}_f''' \otimes \mathbf{u}_f''' \rangle_f$ to $\overline{v_f^2}$ a transport equation can be written as:

$$\frac{\partial(\alpha_f \rho_f \overline{v_f^2})}{\partial t} + \nabla \cdot (\alpha_f \rho_f \overline{v_f^2} \mathbf{u}_f) = \nabla \cdot \left(\mu_f + \frac{\mu_{ft}}{\sigma_{fk}} \right) \nabla \overline{v_f^2} + \overline{v_f^2}_{source} - \alpha_f \rho_f 6 \frac{\overline{v_f^2}}{k_f} \varepsilon_f + 2\beta(\overline{v_{fp}^2} - \overline{v_f^2}). \tag{16}$$

The reader should note that the third term on the RHS is a sink term that is used to balance the source term $k_f f$. This is a modification proposed by Lien and Kalitzin [26] and ensures that the source term $k_f f \rightarrow 0$ as it approaches the wall.

Equation 16 contains no sensitivity to the wall, this is introduced through a modified Helmholtz equation which forms an elliptic relaxation equation. The form of this equation accounts for anisotropy close to walls and is also independent of Reynolds number and y$^+$ value which reads:

$$L^2 \frac{\partial^2 f}{\partial x^2} - f = \underbrace{\frac{C_1}{T} \left(\frac{\overline{v_f^2}}{k_f} - \frac{2}{3} \right)}_{\phi_{yy,S}} - \underbrace{C_2 \frac{\Pi_f}{k_f}}_{\phi_{yy,R}} - \frac{1}{T} \left(6 \frac{\overline{v_f^2}}{k_f} - \frac{2}{3} \right). \tag{17}$$

The terms $\phi_{yy,S}$ and $\phi_{yy,R}$ are the so-called slow and rapid pressure-strain terms [22, 33] with the final term being used to ensure far field behaviour i.e. that the elliptic relaxation function diminishes away from walls.

In the original formulation of this equation as given by Durbin [8] the boundary condition for f contains the wall distance to the fourth power in its denominator. This lead to computational stiffness and numerical oscillations in the near-wall region. This issue was resolved by Lien and Kalitzin [26] by introducing $6\frac{\overline{v_f^2}}{k_f}$ as a sink and source in the $k_f f$ source term, the $\overline{v_f^2}$ transport equation and the elliptical relaxation equation, f. This ensures that f tends to 0 at the wall enabling a Dirichlet boundary condition to be prescribed. The turbulent viscosity is calculated from the solution of the $\overline{v_f^2} - f$ model and a correction is employed to ensure the correct velocity scale is used as the wall is approached. The correction of Davidson et al. [7] is employed and the definition of the turbulent viscosity now reads

$$\nu_{ft} = \min\Big\{C_{f\mu} k_f^2/\varepsilon_f,\ C_\mu \overline{v_f^2} T\Big\}, \tag{18}$$

where the turbulent time and length scales are defined as

$$T = \max\left(\frac{k_f}{\varepsilon_f}, 6\sqrt{\frac{\nu_f}{\varepsilon_f}}\right), \tag{19}$$

$$L = \max\left(\frac{k_f^{3/2}}{\varepsilon_f}, C_\eta \frac{\nu_f^{3/4}}{\varepsilon_f^{1/4}}\right). \tag{20}$$

Both time and length scales are limited in regions close to the wall. This is achieved by introducing a dependency on Kolmogorov scales which are only active in regions very close to the wall i.e. $y^+ < 5$. This ensures that a singularity is not introduced into the solution matrix and that the scales collapse at the wall. Another modification close to the wall is to modify the "constant" $C_{\varepsilon 1}$ by damping it in the near-wall region by employing the following formulation

$$C_{\varepsilon 1} = 1.4\Big(1 + 0.05\sqrt{k_f/\overline{v_f^2}}\Big). \tag{21}$$

To summarise, the $\overline{v_f^2} - f$ model equations can be found in Table 4 with the turbulence modelling constants, taken from the original model [8], found in Table 8. The complete set of equations that make up the RA-TFM with the $\overline{v_f^2} - f$ model is then the equations found in Table 1 and the aforementioned equations.

Table 4: $\overline{v_f^2} - f$ model equations.

$$\frac{\partial(\alpha_f \rho_f k_f)}{\partial t} + \nabla \cdot (\alpha_f \rho_f k_f \mathbf{u}_f) = \nabla \cdot \left(\mu_f + \frac{\mu_{ft}}{\sigma_{fk}}\right) \nabla k_f + \alpha_f \rho_f \Pi_f - \alpha_f \rho_f \varepsilon_f + 2\beta(k_{fp} - k_f) \tag{22}$$

$$\frac{\partial(\alpha_f \rho_f \varepsilon_f)}{\partial t} + \nabla \cdot (\alpha_f \rho_f \varepsilon_f \mathbf{u}_f) = \nabla \cdot \left(\mu_f + \frac{\mu_{ft}}{\sigma_{f\epsilon}}\right) \nabla \varepsilon_f + \frac{\varepsilon_f}{k_f}\left[\frac{C_{\varepsilon 1} \alpha_f \rho_f \Pi_f - C_{\varepsilon 2} \alpha_f \rho_f \varepsilon_f}{T}\right] + 2C_3\beta(\varepsilon_{fp} - \varepsilon_f) \tag{23}$$

$$\frac{\partial(\alpha_f \rho_f \overline{v_f^2})}{\partial t} + \nabla \cdot (\alpha_f \rho_f \overline{v_f^2} \mathbf{u}_f) = \nabla \cdot \left(\mu_f + \frac{\mu_{ft}}{\sigma_{fk}}\right) \nabla \overline{v_f^2} + \overline{v^2_f}_{source} - \alpha_f \rho_f 6 \frac{\overline{v_f^2}}{k_f} \varepsilon_f + 2\beta(\overline{v_{fp}^2} - \overline{v_f^2}) \tag{24}$$

$$L^2 \frac{\partial^2 f}{\partial x^2} - f = \frac{C_1}{T}\left(\frac{\overline{v_f^2}}{k_f} - \frac{2}{3}\right) - C_2 \frac{\Pi_f}{k_f} - \frac{1}{T}\left(6\frac{\overline{v_f^2}}{k_f} - \frac{2}{3}\right) \tag{25}$$

Table 5: $\overline{v_f^2} - f$ model parameters.

C_μ	C_1	C_2	C_L	C_η	$C_{\varepsilon 2}$	C_3	β_k	β_ϵ	β_v	$C_{f\mu}$	σ_k	$\sigma_{f\epsilon}$
0.22	1.4	0.3	0.23	70	1.9	1	1	1	1	0.09	1	1.3

Wall boundary conditions for ε_f can be found by a Taylor expansion around the no-slip condition at the wall [33] which reads as:

$$\varepsilon_f \to 2\nu_f \frac{k_f}{\mathrm{y}^2} \tag{26}$$

For the remaining fluid-phase model variables the following boundary conditions at the wall are prescribed, $\mathbf{u}_f = k_f = \overline{v_f^2} = f = 0$. For the particulate phase a Neumann boundary condition is prescribed for the velocity and all turbulence statistics. For the simulations with the $k_f - \varepsilon_f$ model the standard wall functions for both turbulence statistics are employed. At the inlet the velocity of both the fluid- and particle-phase are set at 9.4ms^{-1}. A Neumann boundary condition is used for f together with Dirichlet boundary conditions for all turbulent statistics. At the outlet the a Dirichlet boundary condition for pressure is set whilst a Neumann boundary condition is prescribed for all remaining variables. Both k_p and ε_p are initialised as 1/3rd of their fluid counterpart with $\Theta_p = 1.0 \text{ x } 10^{-8}\text{m}^2\text{s}^{-2}$.

The RA-TFM and the recently derived $\overline{v_f^2} - f$ turbulence model is implemented into the open-source toolbox OpenFOAM [53] and is denoted as `ratfmFoam` [36, 37] which is made available for public use. To handle the pressure-velocity coupling the Pressure Implicit with Splitting Operators (PISO) algorithm [10, 17] is used. The volume fraction is solved using Multi-dimensional Universal Limiter with Explicit Solution (MULES) [56] which is a flux-corrected transport algorithm which ensures robustness, stability and convergence. Time derivative terms are discretised using the first order accurate implicit Euler, gradients are discretised using the Gauss-Green scheme, convective terms are discretised using the first-order upwind scheme Finally, Laplacian schemes are discretised with the second order accurate central differencing scheme.

2.2. Simulation cases

Table 6: Table of simulated cases

Case	Material	d_p [μm]	ρ_p [kg m^{-3}]	Mass loading, ϕ	St
1	glass	50	2500	2%	0.57
2	copper	70	8800	10%	3

The cases used throughout are based on two experiments from Kulick et al. [20] which include separately both glass and copper particles, the details of which can be found in Table 6. For both cases the the channel half-width is H = 0.02m with a corresponding length of 5.2m and a wall friction velocity $u_\tau = 0.49$ms^{-1}. The viscosity of gas is $\nu_f = 15.11$ x 10^{-5}m^{2}s^{-1} with a density of $\rho_f = 1.2$kg m^{-3} The flow is orientated vertically with a uniform body force of gravity acting in the direction of the flow (g = 9.8m s^{-2}), this configuration resulted in a centerline velocity of $U_{cl} = 10.5$ms^{-1}. The mass loading is defined as $\phi = \frac{\alpha_p \rho_p}{\alpha_f \rho_f}$, and assuming uniform velocity at the inlet.

Table 7: Properties of each mesh, f_x, f_y refer to mesh stretching with Mesh 1 [$f_x = 1.1, f_y = 1.1$] and Mesh 2 [$f_x = 1.2, f_y = 1.2$].

Mesh	$\Delta x_{min}, \Delta x_{max}$[m]	$\Delta y_{min}, \Delta y_{max}$[m]	Mesh size	Comp time
1	1.2×10^{-3}, 0.02	1.2×10^{-5}, 1.2×10^{-3}	202,761	32 hrs
″	″	″	″	20 hrs
2	7×10^{-4}, 9×10^{-4}	7×10^{-4}, 9×10^{-4}	66,481	4 hrs

Owing to the different modelling approaches used throughout two different meshes are employed and are detailed in Table 7. Mesh 1 is associated with the $\overline{v_f^2} - f$ model and the low Re Number model of Launder and Sharma [21] and is resolved to y$^+ < 1$

ensuring that the resolution of the boundary layer is captured. Mesh 2 is associated with the $k_f - \varepsilon_f$ model and is resolved up to y$^+ > 30$ ensuring that the wall functions can be applied across the correct section of the boundary layer (i.e. log-layer). The final column refers to the computational time spent for a typical run consisting of 30 seconds of real flow time. For ease of reference the $\overline{v_f^2} - f$ formulation will hereafter be referred to as V2F, the low Re number formulation as LE and the $k_f - \varepsilon_f$ formulation as KE.

3. Results and Discussion

3.1. Mean fluid stream-wise velocity profiles

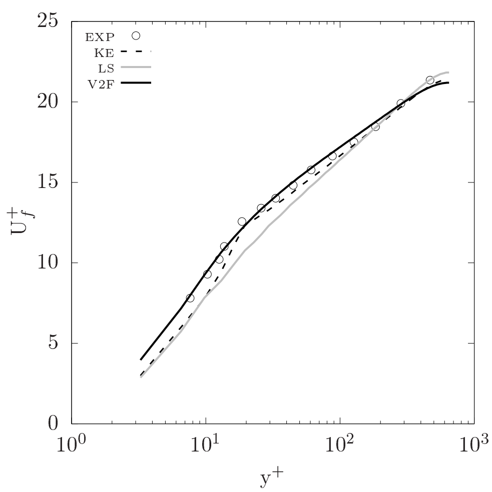

Figure 1: C1 - Mean fluid velocity profile.

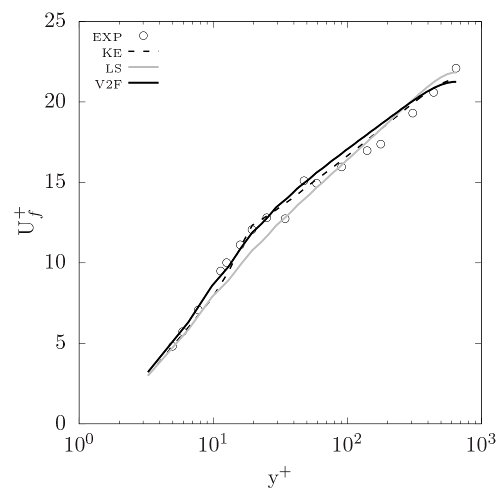

Figure 2: C2 - Mean fluid velocity profile.

Figures 1 & 2 show the mean fluid velocity profiles for each case. It is evident from both plots that the prediction of both V2F & KE models are in good agreement with the experimental data of Kulick et al. [20]. For both C1 & C2 the mean fluid velocity profile remains unchanged, behaviour that is consistent with the experimental observations. Moreover, the experimental uncertainty was reported by the authors to be $\approx 2\%$ and it can be seen that across both profiles the numerical prediction lies well within this range.

This behaviour is not apparent in the predictions from the LE model as there is an underestimation of the fluid velocity. It is interesting to observe that the LE and KE predictions are similar outside the range of $10 < y^+ < 100$ across both plots. Over the transition region i.e. buffer layer to log-layer, the damping function tends to over-predict the turbulence viscosity. The ‘kink’ is not reproduced leading to a flattening of the velocity profile but despite this the overall prediction is satisfactory.

When comparing both the V2F & KE model predictions there is only a small discrepancy between each result. This disparity is at its most obvious across the viscous and buffer layer i.e. $y^+ < 20$ in Fig. 1. Owing to the wall function the turbulence statistics are integrated to the wall, with a presumed log-layer relationship, from the first computational cell at $y^+ \approx 30$. This resulted in an over-prediction of turbulence viscosity which is felt as an under-prediction in the mean velocity profile. This trend is seen across the profile for both plots as the KE consistently under-predicts the mean velocity profile in comparison with V2F although this difference is small.

3.2. Mean particle stream-wise velocity profiles

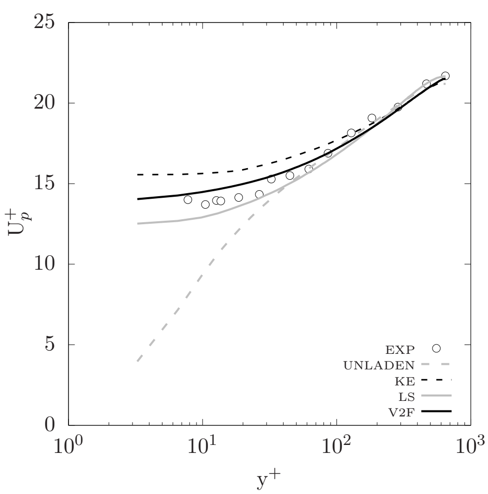

Figure 3: C1 - Mean particle velocity profile.

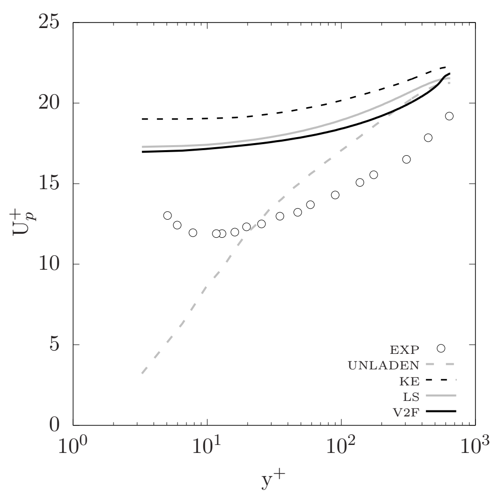

Figure 4: C2 - Mean particle velocity profile.

The mean particle velocity profiles are shown in Figs. 3 & 4. Focusing on the former it can be seen that V2F, LE & KE models accurately predict the trend seen in the experimental observations. The trend is characterised by a flatter profile as the particles approach the wall. As the particle velocities need not be zero at the wall unlike in the fluid-phase, a large slip value exists. The particles deviate from the fluid-phase velocities at around $y^+ < 100$ and maintain their momentum, leading to a flattening of the profile as the wall is approached.

In Fig. 3 the profile predicted by the V2F model is in good agreement with the experimental data. This is also true for the KE and LE models up until the near-wall region is approached. Over the range $y^+ < 100$ the KE prediction deviates from the experimental results as the momentum is over-predicted. The contrary is true for the LE model in which the particles remain correlated with the carrier flow up until $y^+ \approx 50$ and then begin to deviate resulting in a under-estimation of the particle velocities. The cause of this behaviour is attributed to the particle fluctuation energy calculation. For the KE model this results is an underestimation of the energy exchange and for the LE model an overestimation, this behaviour will be discussed further in Sec. 3.5.

Looking at Fig. 4 it can be seen that there is an over-estimation in the mean particle velocities across all three models. This discrepancy was also predicted in the E-L results of Yamamoto et al. [54] and Wang and Squires [52]. A recent study by Vreman [51] suggests that this global reduction in the particle velocities is due to the so-called "non-uniform feedback force" which is exacerbated by wall roughness. This results in an additional drag force exerted on the particles leading to increased turbulence attenuation.

This additional force would result in a much flatter profile as shown in Vreman

[51] and lead to results that closely align with the experimental data in Fig. 4. As wall roughness has not been modelled in this study, and similar results have been reported by other researchers using higher resolution methods i.e. E-L [54, 52], it is plausible to conclude that this is the source of the overestimation. It is instructive to note that despite this, the qualitative behaviour of the profile is captured by the numerical models resulting in a comparable trend across the profile.

3.3. *Fluid stream-wise turbulence intensity*

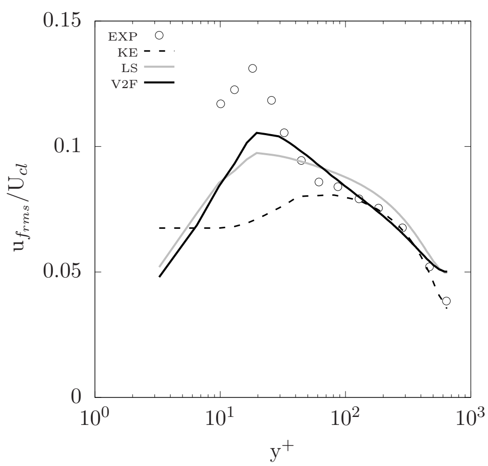

Figure 5: C1 - Fluid stream-wise turbulence intensity profile.

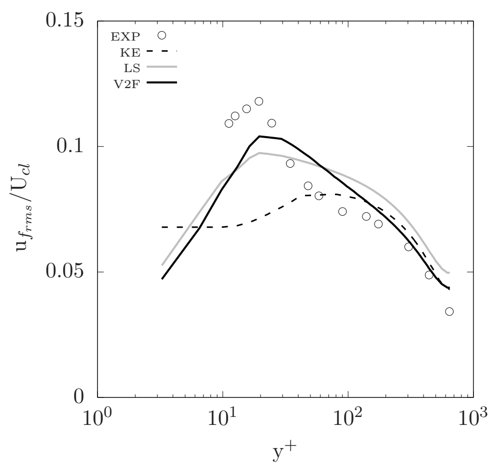

Figure 6: C2 - Fluid stream-wise turbulence intensity profile.

Figures 5 & 6 show the fluid-phase turbulence intensity for each case. When comparing the V2F & KE model across both cases it is apparent that there is a clear difference between the two. The V2F model is capable of predicting a strong peak at $y^+ \approx 20$ and then dissipating off into the core of the channel. This is, of course, not seen in the KE model result as the first computational cell is placed at $y^+ > 30$.

This then omits the presence of the peak and results in a near constant value of $u_{f_{rms}}$ as the wall is approached. In the core of the flow, over the region ($y^+ > 70$), there is better agreement with the experimental data as the transport terms begin to dominate.

The LE model performs well in comparison with the experimental data. Resolving the near wall region enables the peak to be predicted although it is not as pronounced or concentrated as the peak predicted by the V2F model. There is a "spreading" of the turbulent kinetic energy across the range, $10 < y^+ < 100$, smearing the transition region. This is suspected to be the cause of the degradation of the mean velocity profile in Figs. 1 & 2. This could be improved through tweaking of the damping function but as highlighted in the introduction this is an inherit shortcoming of the approach and there are several different ad-hoc solutions to dampening the viscosity but the underlying issues remain.

The KE models dependency on the wall function results in a deterioration of the turbulence intensity prediction. This will be shown to have important consequences when predicting the particle fluctuation energy behaviour. The V2F model shows excellent agreement across both plots with the under prediction being confined to the turbulence peak and dissipation towards the wall. It has been suggested [9, 8] that the $\overline{v_f^2} - f$ model performs best at high Re number. In this work a relatively low Re number of 14,000 is simulated which could be the cause of the under-prediction. This could be improved with a manipulation of the turbulence constant i.e. C_2 although this remains out of the scope of this study.

Kulick et al. [20] reports turbulence attenuation in C2. As discussed in Sec. 3.2

this is due to the lack of wall roughness modelled in this work. Across both Figs. the behaviour is similar with the velocity covariance terms contributing little to the prediction. This finding is also consistent with those of Yamamoto et al. [54], Wang and Squires [52] in which negligible attenuation was reported.

3.4. Fluid wall-normal turbulence intensity

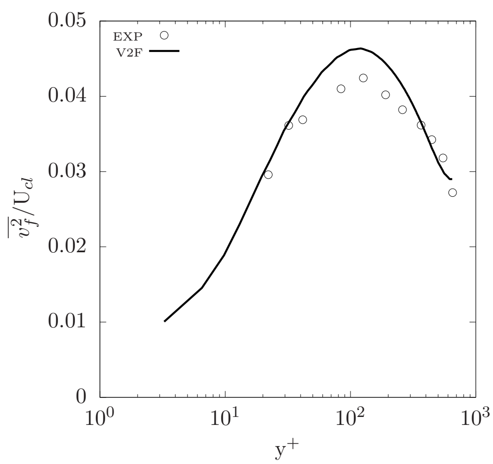

Figure 7: C1 - Fluid wall-normal turbulence intensity profile.

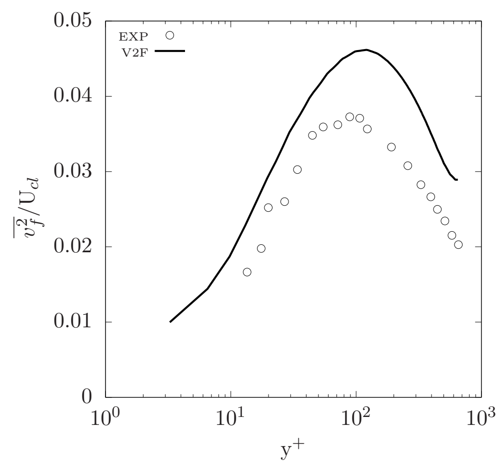

Figure 8: C2 - Fluid wall-normal turbulence intensity profile.

Figures 7 & 8 show the fluctuating wall-normal component. This component is explicitly modelled in the V2F model as $\overline{v_f^2}$ and is crucial in enabling the resolution of the boundary layer. As it can be seen from Fig. 7 the distribution is in good agreement with the experimental predictions. The V2F model shows the correct dampening of the wall-normal component through the elliptic relaxation equation and enables a strong turbulence production peak as seen in Sec. 3.3. For C2 the wall-normal intensity was also attenuated in the same way the stream-wise intensity was. As previously discussed no attenuation was reported in these results.

3.5. *Particle fluctuation energy*

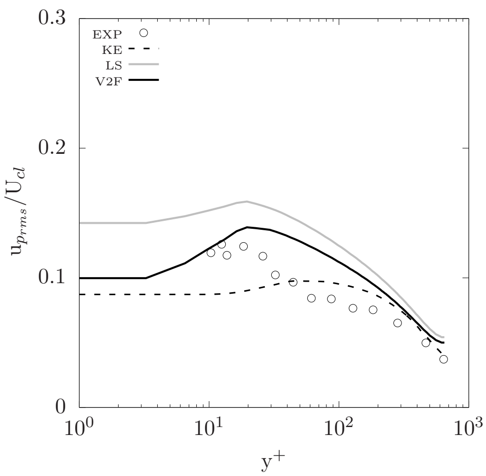

Figure 9: C1 - Particle fluctuation energy profile.

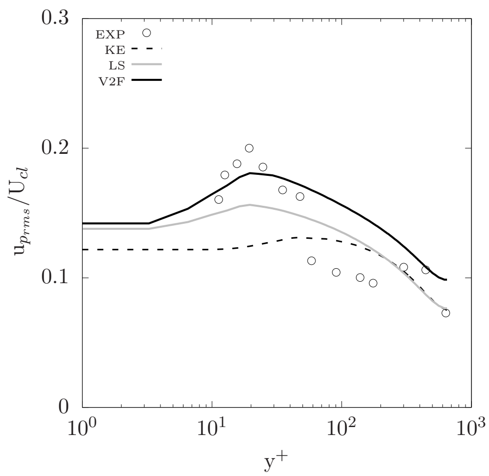

Figure 10: C2 - Particle fluctuation energy profile.

In the RA-TFM we explicitly account for two contributions to the particle fluctuation energy [12], $\kappa_p = 3\Theta_p + k_p$ where Θ_p represents the small-scale kinetic collisional energy i.e. uncorrelated energy and k_p represents the large-scale turbulent kinetic energy i.e. correlated energy. Broadly speaking Θ_p is relevant at high St number and high mass loading, and k_p is relevant at low St number and low mass loading. This distinction has already proven crucial in the literature [12, 18, 38, 39, 50].

Figures 9 & 10 show the particle fluctuation energy for each case. As is evident from both plots the V2F model outperforms the KE model. This is a direct consequence of the poor prediction in the fluid turbulent kinetic energy. Owing to the relatively low St number in the core of the flow the particles are tightly correlated therefore they are governed by the velocity covariance term which arises due to coupling through drag. The fluctuation energy distribution is dominated by k_p up until the near-wall region is approached - this is confirmed by comparing the distribution with that of Fig. 5. For C2 this is not strictly true as the St number is larger in the core of the flow resulting in a contribution acting across the half-width of the channel, this can be seen by comparing the two figures.

In the near-wall region the St number increases dramatically. This ensures that the particles become uncorrelated with the main carrier flow and Θ_p is produced in the region $y^+ < 10$. Additionally, an energy cascade exists in which the large-scale particle turbulent kinetic energy dissipation, ε_p appears in the Θ_p transport equation through a source term. The particle turbulence kinetic energy dissipation is then highest in the near-wall region thus contributing to the loss of correlation with the carrier flow.

The LE model overestimates the fluctuation energy in C1 and the profile begins to flatten out as the wall is approach. As shown in §3.2, the particle velocity profile was under predicted which is in line with the behaviour of the particle fluctuation energy. This was caused by an overproduction of Θ_p as the energy transfer was overproduced, this resulted in an excessively large value of Θ_p in the near-wall region. It is not obvious why this occurred as the velocity profile predicted for C2 is in good agreement with the experimental data. It can be speculated that the source of the error is the velocity covariance term as we set the correlation factor to 1 or the kinetic theory constitutive equations as we have employed standard expressions from the literature, although this is far from conclusive.

3.6. Volume fraction distribution

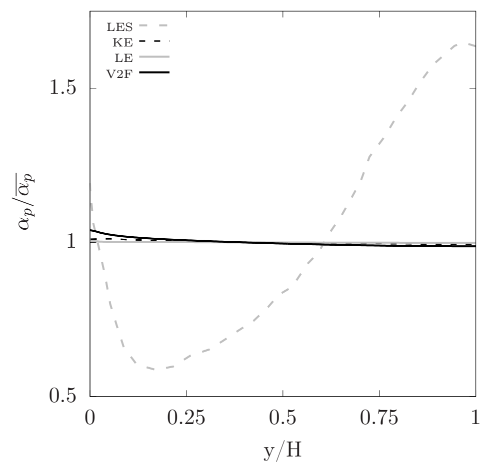

Figure 11: C1 - Volume fraction distribution normalised by mean values. The E-L results of Yamamoto et al. [54] displaying the normalised particle number density function.

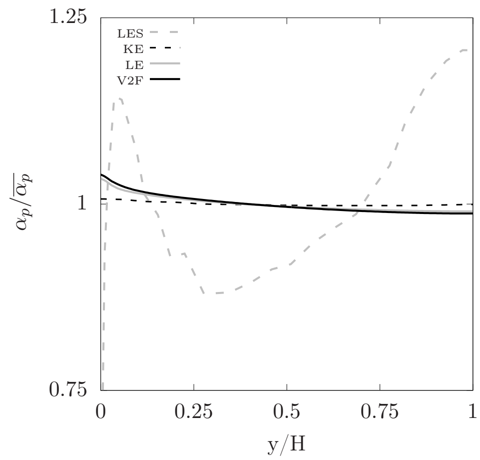

Figure 12: C2 - Volume fraction distribution normalised by mean values. The E-L results of Yamamoto et al. [54] displaying the normalised particle number density function.

Figures 11 & 12 show the volume fraction distribution for both cases. Additionally, the E-L results of Yamamoto et al. [54] have been displayed for qualitative understanding. Across both plots the predictions found herein are at odds with the E-L results. Some similarities can be drawn e.g. an accumulation in the near-wall region in C2 but in general it is difficult to draw any conclusions from the data. The volume fraction is a difficult statistic to predict in E-L and E-E simulations so this result is not unexpected.

It is clear from both plots that the V2F model predicts an accumulation of particles in the near-wall. The particles tend to drift across the channel width and reside in the near-wall region - characteristic behaviour of turbophoresis. As the force is determined by the fluctuating wall normal component, of which is explicitly modelled in the V2F model and coupled to the particle-phase correlated energy, the particles are able to drift down the gradients of turbulent kinetic energy.

The KE model predictions reveal a slightly different picture. In C1 an accumulation of particles in the near-wall region is seen but the sharp peak is not replicated, instead these particles are found in the main core of the flow. The prediction for C2 reveals a breakdown in the volume fraction distribution in comparison to the V2F model. The particles are nearly uniformly distributed with a higher concentration in the main core of the flow. Due to the higher St number in C2 the particles are less correlated with the carrier flow, therefore in order to migrate towards the wall a larger dispersion is required. As the wall-normal component has not been explicitly modelled the particles can not overcome the turbulent kinetic energy gradient and remain in the main core of flow. Moreover, this can be a symptom of the mesh resolution as the wall function constraint ensures the near-wall region can not be resolved. The LE model results show no accumulation for C1 but do so for C2. The second result corroborates the findings from the V2F model in that the resolution of the boundary layer can lead to an accumulation of particles in the boundary layer.

4. Conclusions

This work has proposed a generic approach for accounting for near-wall induced non-homogeneity in Eulerian-Eulerian simulations. An E-E elliptic relaxation model, namely the $\overline{v_f^2} - f$ model, has been derived with in a Reynolds-Averaged Two-Fluid model framework and applied to a downward-facing vertical channel. Predictions are validated against the benchmark experimental data of Kulick et al. [20] and compared against the conventional $k_f - \varepsilon_f$ turbulence model. From this work the following conclusions can be drawn:

1. The E-E elliptic relaxation model shows improved prediction of fluid- and particle-phase turbulence statistics when compared with the conventional $k_f - \varepsilon_f$ formulation;
2. The new modelling has been validated against benchmark experimental data with differing mass loading and Stokes number as well as being corroborated with Euler-Lagrange results;
3. The elliptic relaxation model has shown a high level of validation, in line with those from Euler-Lagrange, offering a viable way of achieving accurate results at a lower computational cost;
4. The use of single-phase wall functions in E-E simulations can result in an under-prediction of the velocity covariance coupling term which impedes on the particle fluctuation energy prediction. This is expected to be exacerbated with increasing mass loading;
5. The elliptic relaxation model enabled the migration of particles towards the

near-wall region, a result that was not replicated using the conventional turbulence model;

6. The approach presented herein offers a novel way of accounting for the near-wall region in E-E simulations.

5. Code repository

The source code of the `ratfmFoam` solver and the supplementary data used in this work can be downloaded from [36].

6. Acknowledgements

This work has benefited from a PhD Scholarship from the College of Engineering, Mathematics and Physical Sciences at the University of Exeter. The authors would also like to acknowledge the time used on ISCA HPC and Advanced Computing Facility at the University of Exeter.

7. Appendix

We begin at the fluid-phase momentum equation derived from a collisional Boltzmann equation like the one presented in Fox [13]. Here we couple the phases through drag and include a body force due to gravity. This results in the equation,

$$\frac{\partial(\alpha_f \mathbf{u}_f)}{\partial t} + \nabla \cdot (\alpha_f \mathbf{u}_f \otimes \mathbf{u}_f + \alpha_f \overline{\mathbf{P}}_f) = \frac{\alpha_p \rho_p}{\rho_f} \mathcal{A} + \alpha_f \mathbf{g} \tag{27}$$

Taking the Reynolds-Average (RA) of Eq. 27 gives:

$$\begin{aligned}\frac{\partial \langle\alpha_f\rangle\langle\mathbf{u}_f\rangle_f}{\partial t} + \nabla \cdot \Big(\langle\alpha_f\rangle\langle\mathbf{u}_f\rangle_f \otimes \langle\mathbf{u}_f\rangle_f + \langle\alpha_f\rangle\langle\mathbf{u}''_f \otimes \mathbf{u}''_f\rangle_f + \langle\alpha_f\rangle\langle\overline{\mathbf{P}}_f\rangle\Big) \\ = \frac{\langle\alpha_p\rangle\rho_p}{\rho_f}\langle\mathcal{A}\rangle_f + \langle\alpha_f\rangle\mathbf{g}\end{aligned} \tag{28}$$

where $\langle\alpha_f\rangle$ represents the RA fluid-phase volume fraction and $\langle\mathbf{u}_f\rangle_f = \langle\alpha_f \mathbf{u}_f\rangle / \langle\alpha_f\rangle$ is the Phase-Averaged (PA) fluid-phase velocity. Now grouping the stress terms as, $\langle\overline{\mathcal{P}}_f\rangle_f = \langle\overline{\mathbf{P}}_f\rangle_f + \langle\mathbf{u}'''_f \otimes \mathbf{u}'''_f\rangle_f$ and multiplying through by the PA fluid-phase velocity one arrives at:

$$\begin{aligned}\frac{\partial \langle\alpha_f\rangle\langle\mathbf{u}_f\rangle_f \otimes \langle\mathbf{u}_f\rangle_f}{\partial t} + \nabla \cdot \Big(\langle\alpha_f\rangle\langle\mathbf{u}_f\rangle_f \otimes \langle\mathbf{u}_f\rangle_f \otimes \langle\mathbf{u}_f\rangle_f + \langle\alpha_f\rangle\langle\mathbf{u}_f\rangle_f \otimes \langle\overline{\mathcal{P}}_f\rangle_f\Big) \\ = \frac{\langle\alpha_p\rangle\rho_p}{\rho_f}\langle\mathbf{u}_f\rangle_f \otimes \langle\mathcal{A}\rangle_f + \langle\alpha_f\rangle\langle\mathbf{u}_f\rangle_f \otimes \mathbf{g}\end{aligned} \tag{29}$$

As we want to derive an equation for the Reynolds stress tensor we now find the transport equation for the fluid-phase velocity tensor product. Note this is prior to Reynolds-Averaging. Beginning at Eq. 27 we can multiply through by the fluid-phase velocity, which reads as:

$$\frac{\partial(\alpha_f \mathbf{u}_f \otimes \mathbf{u}_f)}{\partial t} + \nabla \cdot (\alpha_f \mathbf{u}_f \otimes \mathbf{u}_f \otimes \mathbf{u}_f + \alpha_f \mathbf{u}_f \otimes \overline{\mathbf{P}}_f) = \frac{\alpha_p \rho_p}{\rho_f} \mathbf{u}_f \otimes \mathcal{A} + \alpha_f \mathbf{u}_f \otimes \mathbf{g} \tag{30}$$

Now invoking the relation for the fluid-phase pressure-stress tensor,

$$\overline{\mathbf{P}}_f = \frac{1}{\rho_f \alpha_f}(p_f \mathbf{I} - \overline{\boldsymbol{\sigma}}_f), \qquad \langle \overline{\mathbf{P}}_f \rangle = \frac{1}{\rho_f \alpha_f}(\langle p_f \rangle \mathbf{I} - \langle \overline{\boldsymbol{\sigma}}_f \rangle) \tag{31}$$

and the momentum coupling,

$$\mathcal{A} = \frac{1}{\tau_p}(\mathbf{u}_p - \mathbf{u}_f), \qquad \langle \mathcal{A} \rangle_f = \frac{1}{\tau_p}(\langle \mathbf{u}_p \rangle_f - \langle \mathbf{u}_f \rangle_f) \tag{32}$$

and then subtracting Eq. 29 from the RA of Eq. 30, the transport equation for the fluid-phase Reynolds-Stress can be written as

$$\begin{aligned} \frac{\partial \langle \alpha_f \rangle \langle \mathbf{u}_f''' \otimes \mathbf{u}_f''' \rangle_f}{\partial t} + \nabla \cdot \langle \alpha_f \rangle \langle \mathbf{u}_f \rangle_f \otimes \langle \mathbf{u}_f''' \otimes \mathbf{u}_f''' \rangle_f = -\nabla \cdot \langle \alpha_f \rangle \langle \mathbf{u}_f''' \otimes \mathbf{u}_f''' \otimes \mathbf{u}_f''' \rangle_f \\ - \underbrace{\langle \alpha_f \rangle (\langle \mathbf{u}_f''' \otimes \mathbf{u}_f''' \rangle_f \cdot \nabla \langle \mathbf{u}_f \rangle_f)}_{\text{Production}} + \frac{1}{\rho_f} \nabla \cdot \langle \overline{\boldsymbol{\sigma}}_f \otimes \mathbf{u}_f''' \rangle - \frac{1}{\rho_f} \nabla \langle p_f \mathbf{u}_f''' \rangle \\ + \underbrace{\frac{1}{\rho_f} \langle p_f \nabla \mathbf{u}_f''' \rangle}_{\text{pressure strain, } \phi_{yy}} - \underbrace{\frac{1}{\rho_f} \langle \overline{\boldsymbol{\sigma}}_f \cdot \nabla \mathbf{u}_f''' \rangle}_{\text{dissipation, } \varepsilon_{yy}} + \langle \alpha_f \rangle \beta (\underbrace{\langle \mathbf{u}_f''' \otimes \mathbf{u}_p'' \rangle_p - \langle \mathbf{u}_f''' \otimes \mathbf{u}_f''' \rangle_p}_{\text{velocity correlations}}) \end{aligned} \tag{33}$$

where the fluid-phase velocity fluctuations are defined as $\mathbf{u}_f''' = \mathbf{u}_f - \langle \mathbf{u}_f \rangle_f$.

Nomenclature

U_{cl}	centreline velocity, [ms^{-1}]
C_D	drag coefficient, [$-$]
$\mathbf{g}$	gravity, [ms^{-2}]
$\mathbf{n}$	unit vector normal to the wall, [$-$]
Re_p	particle Reynolds number, [$-$]
d_p	particle diameter, [m]
$\mathbf{u}_i$	velocity, [ms^{-1}]
$\mathbf{u}_p''$	particle velocity fluctuation w.r.t PA velocity, [ms^{-1}]
$\mathbf{u}_f'''$	fluid velocity fluctuation w.r.t PA velocity, [ms^{-1}]
p_i	pressure, [Pa]
g_0	radial distribution coefficient, [$-$]
t	time, [s]
k_i	turbulent kinetic energy, [$\mathrm{m}^2\mathrm{s}^{-2}$]

Greek letters

α_i	volume fraction, [$-$]
$\alpha_{p,max}$	maximum particle volume fraction, [$-$]
β	momentum exchange coefficient, [$\mathrm{kgm}^{-3}\mathrm{s}^{-1}$]
$\Delta\mathrm{x}$	length of the cell in the x direction, [m]
$\Delta\mathrm{y}$	length of the cell in the y direction, [m]
ε_i	turbulent kinetic energy dissipation, [$\mathrm{m}^2\mathrm{s}^{-3}$]
Θ_p	granular temperature, [$\mathrm{m}^2\mathrm{s}^{-2}$]
κ_p	particle fluctuation energy, [$\mathrm{m}^2\mathrm{s}^{-2}$]
$\kappa_{\Theta s}$	diffusion coefficient for granular energy, [$\mathrm{kgm}^{-1}\mathrm{s}^{-1}$]
μ_i	shear viscosity, [$\mathrm{kgm}^{-1}\mathrm{s}^{-1}$]
$\mu_{i,t}$	turbulent shear viscosity, [$\mathrm{kgm}^{-1}\mathrm{s}^{-1}$]
ν_i	kinematic viscosity, [$\mathrm{m}^2\mathrm{s}^{-1}$]
$\nu_{i,t}$	turbulent kinematic viscosity, [$\mathrm{m}^2\mathrm{s}^{-1}$]
ρ_i	density, [kgm^{-3}]
$\overline{\boldsymbol{\sigma}}_f$	fluid phase stress tensor,[$\mathrm{kgm}^{-1}\mathrm{s}^{-2}$]
$\overline{\boldsymbol{\sigma}}_p$	particle phase stress tensor, [$\mathrm{kgm}^{-1}\mathrm{s}^{-2}$]
τ_p	particle relaxation time, [s]
τ_f	characteristic flow time, [s]

Subscripts

f	fluid
i	general index
p	particle
x	x direction
y	y direction
yy	wall normal component
z	z direction

Superscripts

$''$	PA particle velocity fluctuation
$'''$	PA fluid velocity fluctuation

Special notation

$\langle \cdot \rangle$	Reynolds averaging operator
$\langle \cdot \rangle_i$	phase averaging operator associated with phase i

Table 8: Model characteristics & turbulence variables.

$$\beta = \frac{\rho_p \alpha_p}{\tau_d} = \frac{3}{4} \frac{\alpha_p \alpha_f \rho_f \mathbf{u}_r}{d_p} C_d$$

$$C_d = \begin{cases} \frac{24}{Re_p}\left[1 + 0.15 Re_p^{0.287}\right] & \text{if } Re_p < 1000 \\ 0.44 & \text{if } Re_p \geq \ 1000 \end{cases}$$

$$\kappa_p = k_p + 3/2\Theta_p$$

$$u_{p_{rms}} = \sqrt{(2/3)\kappa_p}$$

$$u_{f_{rms}} = \sqrt{(2/3)k_f}$$

$$\tau_p = \frac{\rho_p d_p^2}{18 \rho_f \nu_f}$$

$$\tau_f = \frac{k_f}{\varepsilon_f}$$

$$St = \tau_d/\tau_f$$

$$e = 0.9$$

$$\Pi_p = 2\nu_{pt} \overline{\mathbf{S}}_\mathbf{p} : \overline{\mathbf{S}}_\mathbf{p} + \frac{2}{3} k_p \nabla \cdot \mathbf{u}_p$$

$$\Pi_f = 2\nu_{ft} \overline{\mathbf{S}}_\mathbf{f} : \overline{\mathbf{S}}_\mathbf{f} + \frac{2}{3} k_f \nabla \cdot \mathbf{u}_f$$

Table 9: Definition of variables.

$$\kappa_p = k_p + 1.5\Theta_p$$

$$\mu_f = \rho_f \nu_f$$

$$\mu_{ft} = \alpha_f \rho_f \nu_{ft} = \alpha_f \rho_f C_{f\mu} \frac{k_f^2}{\varepsilon_f}$$

$$\mu_p = \alpha_p \rho_p \nu_p = \frac{2\mu_{p_{dil}}}{(1+e)g_0}\Big[1 + \frac{4}{5}(1+e)g_0\alpha_p\Big]^2 + \frac{4}{5}\alpha_p^2 \rho_p d_p g_0 (1+e)\Big(\frac{\Theta_p}{\pi}\Big)^{1/2}$$

$$\mu_{p_{dil}} = \frac{5\sqrt{\pi}}{96}\rho_p d_p \Theta_p^{1/2}$$

$$\mu_{pt} = \alpha_p \rho_p \nu_{pt} = \alpha_p \rho_p C_{p\mu} \frac{k_p^2}{\varepsilon_p}$$

$$p_p = \rho_p \alpha_p \Theta_p + 2(1+e)\rho_p \alpha_p^2 g_0 \Theta_p$$

$$\gamma = \frac{12(1-e^2)g_o}{\sqrt{\pi} d_p}\alpha_p^2 \rho_p \Theta_p^{3/2}$$

$$\kappa_\Theta = \frac{2}{(1+e)g_0}\Big[1 + \frac{6}{5}(1+e)g_0\alpha_p\Big]^2 \kappa_{\Theta,dil} + 2\alpha_p^2 \rho_p d_p g_0 (1+e)\Big(\frac{\Theta_p}{\pi}\Big)^{\frac{1}{2}}$$

$$\kappa_{\Theta,dil} = \frac{75}{384}\sqrt{\pi}\rho_p d_p \Theta_p^{1/2}$$

$$g_0 = \Big[1 - \Big(\frac{\alpha_p}{\alpha_{p,max}}\Big)^{\frac{1}{3}}\Big]^{-1}$$

$$\overline{\mathbf{S}}_\mathbf{p} = \frac{1}{2}[\nabla \mathbf{u}_p + (\nabla \mathbf{u}_p)^T] - \frac{1}{3}\nabla \cdot \mathbf{u}_p \mathbf{I}$$

$$\overline{\mathbf{S}}_\mathbf{f} = \frac{1}{2}[\nabla \mathbf{u}_f + (\nabla \mathbf{u}_f)^T] - \frac{1}{3}\nabla \cdot \mathbf{u}_f \mathbf{I}$$

$$k_{fp} = \beta_k \sqrt{k_f k_p}$$

$$\varepsilon_{fp} = \beta_\varepsilon \sqrt{\varepsilon_f \varepsilon_p}$$

8. Bibliography

[1] Behnia, M., Parneix, S., and Durbin, P. (1998). Prediction of heat transfer in an axisymmetric turbulent jet impinging on a flat plate. *International Journal of Heat and Mass Transfer*, 41(12):1845 – 1855.

[2] Benyahia, S., Syamlal, M., and O'Brien, T. J. (2005). Evaluation of boundary conditions used to model dilute, turbulent gas/solids flows in a pipe. *Powder Technology*, 156(2):62 – 72. Particle Technology Forum Special Issue.

[3] Bolio, E. J., Yasuna, J. A., and Sinclair, J. L. (1995). Dilute turbulent gas-solid flow in risers with particle-particle interactions. *AIChE Journal*, 41(6):1375–1388.

[4] Caraman, N., Borée, J., and Simonin, O. (2003). Effect of collisions on the dispersed phase fluctuation in a dilute tube flow: Experimental and theoretical analysis. *Physics of Fluids*, 15(12):3602–3612.

[5] Chien, K.-Y. (1982). Predictions of Channel and Boundary-Layer Flows with a Low-Reynolds-Number Turbulence Model. *AIAA Journal*, 20(1):33–38.

[6] Dasgupta, S., Jackson, R., and Sundaresan, S. (1998). Gas-particle flow in vertical pipes with high mass loading of particles. *Powder Technology*, 96(1):6 – 23.

[7] Davidson, L., Nielsen, P. V., and Sveningsson, A. (2003). Modifications of the v2-f model for computing the flow in a 3d wall jet. In *Turbulence, heat and mass transfer*, pages 577–584.

[8] Durbin, P. A. (1991). Near-wall turbulence closure modeling without "damping functions". *Theoretical and Computational Fluid Dynamics*, 3(1):1–13.

[9] Durbin, P. A. and Reif, B. A. P. (2010). *Statistical theory and modeling of turbulence flow*, pages 109–154. John Wiley & Sons, Ltd.

[10] Ferziger, J. H. and Peric, M. (2002). *Computational Methods for Fluid Dynamics*.

[11] Fessler, J. R. and Eaton, J. K. (1999). Turbulence modification by particles in a backward-facing step flow. *Journal of Fluid Mechanics*, 394(1999):97–117.

[12] Février, P., Simonin, O., and Squires, K. D. (2005). Partitioning of particle velocities in gas–solid turbulent flows into a continuous field and a spatially uncorrelated random distribution: theoretical formalism and numerical study. *Journal of Fluid Mechanics*, 533:1–46.

[13] Fox, R. O. (2014). On multiphase turbulence models for collisional fluid-particle flows. *Journal of Fluid Mechanics*, 742:368–424.

[14] Gidaspow, D. (1994). *Multiphase flow and fluidization.*

[15] Gore, R. and Crowe, C. (1989). Effect of particle size on modulating turbulent intensity. *International Journal of Multiphase Flow*, 15(2):279 – 285.

[16] Hanjalic, K. and Launder, B. (1980). Sensitizing the dissipation equation to irrotational strains. *Journal of Fluids Engineering*, 102(1):34–40.

[17] Issa, R. I. (1986). Solution of the implicitly discretised fluid flow equations by operator-splitting. *Journal of Computational Physics*, 62(1):40–65.

[18] Kaufmann, A., Moreau, M., Simonin, O., and Helie, J. (2008). Comparison between lagrangian and mesoscopic eulerian modelling approaches for inertial particles suspended in decaying isotropic turbulence. *Journal of Computational Physics*, 227(13):6448–6472.

[19] Kubik, A. and Kleiser, L. (2006). Influence of mass loading on particle-laden turbulent channel flow. *PAMM*, 6(1):531–532.

[20] Kulick, J., Fessler, J. R., and Eaton, J. R. (1994). Particle response and turbulence modification in fully developed channel flow. *Journal of Fluid Mechanics*, 277:109–134.

[21] Launder, B. and Sharma, B. (1974). Application of the energy-dissipation model of turbulence to the calculation of flow near a spinning disc. *Letters in Heat and Mass Transfer*, 1(2):131 – 137.

[22] Launder, B. E., Reece, G. J., and Rodi, W. (1975). Progress in the development of a reynolds-stress turbulence closure. *Journal of Fluid Mechanics*, 68(3):537–566.

[23] Lee, S. and Durst, F. (1982). On the motion of particles in turbulent duct flows. *International Journal of Multiphase Flow*, 8(2):125 – 146.

[24] Li, T. (2009). Revisiting the Johnson and Jackson Boundary Conditions for Granular Flows. *IFAC Proceedings Volumes.*

[25] Li, Y., McLaughlin, J. B., Kontomaris, K., and Portela, L. (2001). Numerical simulation of particle-laden turbulent channel flow. *Physics of Fluids*, 13(10):2957–2967.

[26] Lien, F.-S. and Kalitzin, G. (2001). Computations of transonic flow with the v2-f turbulence model. *International Journal of Heat and Fluid Flow*, 22(1):53–61.

[27] Marchioli, C. and Soldati, A. (2002). Mechanisms for particle transfer and segregation in a turbulent boundary layer. *Journal of Fluid Mechanics*, 468:283–315.

[28] Mito, Y. and Hanratty, T. J. (2006). Effect of feedback and inter-particle collisions in an idealized gas-liquid annular flow. *International Journal of Multiphase Flow*, 32(6):692 – 716.

[29] Ooi, A., Iaccarino, G., Durbin, P., and Behnia, M. (2002). Reynolds averaged simulation of flow and heat transfer in ribbed ducts. *International Journal of Heat and Fluid Flow*, 23(6):750 – 757.

[30] Pan, Y. and Banerjee, S. (1996). Numerical simulation of particle interactions with wall turbulence. *Physics of Fluids*, 8(10):2733–2755.

[31] Patel, V. C., Rodi, W., and Scheuerer, G. (1985). Turbulence models for near-wall and low Reynolds number flows - A review. *AIAA Journal*, 23(9):1308–1319.

[32] Pedinotti, S. and Mariotti, G. (1992). Direct numerical simulation of particle behaviour in the wall region of turbulent flows in horizontal channels. 18(6):927–941.

[33] Pope, S. B. (2011). *Turbulent flows*. Cambridge Univ. Press, Cambridge.

[34] Rashidi, M., Hetsroni, G., and Banerjee, S. (1990). Particle-turbulence interaction in a boundary layer. *International Journal of Multiphase Flow*, 16(6):935–949.

[35] Reeks, M. (1983). The transport of discrete particles in inhomogeneous turbulence. *Journal of Aerosol Science*, 14(6):729 – 739.

[36] Riella, M. (2019a). ratfmfoam for openfoam-2.2.2. https://doi.org/10.5281/zenodo.2620412.

[37] Riella, M. (2019b). *Turbulence modelling of fluid-particle interaction*. PhD thesis, University of Exeter.

[38] Riella, M., Kahraman, R., and Tabor, G. (2018). Reynolds-averaged two-fluid model prediction of moderately dilute fluid-particle flow over a backward-facing step. *International Journal of Multiphase Flow*, 106:95 – 108.

[39] Riella, M., Kahraman, R., and Tabor, G. (2019). Inhomogeneity and anisotropy in eulerian-eulerian near-wall modelling. *International Journal of Multiphase Flow*, 114:9 – 18.

[40] Rizk, M. A. and Elghobashi, S. E. (1989). A two-equation turbulence model for dispersed dilute confined two-phase flows. *International Journal of Multiphase Flow*, 15(1):119–133.

[41] Rodi, W. and Mansour, N. N. (1993). Low Reynolds number k-epsilon modelling with the aid of direct simulation data. *Journal of Fluid Mechanics*, 250:509–529.

[42] Rouson, D. W. I. and Eaton, J. K. (2001). On the preferential concentration of solid particles in turbulent channel flow. *Journal of Fluid Mechanics*, 428:149–169.

[43] Rumsey, C. L. (2010). Compressibility considerations for kw turbulence models in hypersonic boundary-layer applications. *Journal of Spacecraft and Rockets*, 47(1):11–20.

[44] Saber, A., Lundström, T., and Hellström, J. (2016). Influence of inertial particles on turbulence characteristics in outer and near wall flow as revealed with high resolution particle image velocimetry. *Journal of Fluids Engineering, Transactions of the ASME*, 138(9):1–12.

[45] Schlichting, H., Gersten, K., Krause, E., Oertel, H., and Mayes, K. (1955). *Boundary-layer theory*. Springer.

[46] Shih, T. H. and Hsu, A. T. (1991). An improved k-epsilon model for near wall turbulence. *Center for Modeling of Turbulence and Transition (CMOTT). Research Briefs: 1990*, 1:87–104.

[47] Strömgren, T., Brethouwer, G., Amberg, G., and Johansson, A. V. (2012). Modelling of turbulent gas-particle flows with focus on two-way coupling effects on turbophoresis. *Powder Technology*, 224:36–45.

[48] Sveningsson, A. (2003). Analysis of the Performance of Different v2f Turbulence Models in a Stator Vane Passage Flow. *PhD Thesis*.

[49] Tsuji, Y. and Morikawa, Y. (1984). LDV measurements of an air-solid two-phase flow in a vertical pipe. *Journal of Fluid Mechanics*, 120:385–409.

[50] Vance, M. W., Squires, K. D., and Simonin, O. (2006). Properties of the particle velocity field in gas-solid turbulent channel flow. *Physics of Fluids*, 18(6):063302.

[51] Vreman, A. W. (2015). Turbulence attenuation in particle-laden flow in smooth and rough channels. *Journal of Fluid Mechanics*, 773:103–136.

[52] Wang, Q. and Squires, K. D. (1996). Large eddy simulation of particle-laden turbulent channel flow. *Physics of Fluids*, 8(5):1207–1223.

[53] Weller, H. G., Tabor, G., Jasak, H., and Fureby, C. (1998). A tensorial approach to computational continuum mechanics using object-oriented techniques. *Computers in Physics*, 12(6):620–631.

[54] Yamamoto, Y., Potthoff, M., Tanaka, T., Kajishima, T., and Tsuji, Y. (2001). Large-eddy simulation of turbulent gas-particle flow in a vertical channel: effect of considering inter-particle collisions. *Journal of Fluid Mechanics*, 442:303–334.

[55] Young, J. and Leeming, A. (1997). A theory of particle deposition in turbulent pipe flow. *Journal of Fluid Mechanics*, 340:129–159.

[56] Zalesak, S. T. (1979). Fully multidimensional flux-corrected transport algorithms for fluids. *Journal of Computational Physics*, 31(3):335–362.

[57] Zheng, Y., Wan, X., Qian, Z., Wei, F., and Jin, Y. (2001). Numerical simulation of the gas-particle turbulent flow in riser reactor based on k-ϵ-kp-ϵp-θ two-fluid model. *Chemical Engineering Science*, 56(24):6813–6822.